X-ray microscopy study of chromonic liquid crystal dry film texture

K. V. Kaznatcheev,[1,*] P. Dudin,[1,2] O. D. Lavrentovich,[3] and A. P. Hitchcock[4]
[1]*Canadian Light Source, University of Saskatchewan, Saskatoon, SK S7N 0X4, Canada*
[2]*Sincrotrone Trieste, S.C.p.A., S.S.14 km 163.5 in Area Science Park, I-34012, Basovizza, Trieste, Italy*
[3]*Liquid Crystal Institute, Kent State University, Kent, Ohio 44242, USA*
[4]*BIMR, Department of Chemistry, McMaster University, Hamilton, Ontario, L8S 4M1, Canada*
(Received 8 July 2007; revised manuscript received 20 September 2007; published 26 December 2007)

Soft x-ray spectromicroscopy has been used to investigate the degree of the molecular alignment of sulfonated benzo[de]benzo[4.5]imidazo[2,1-a]isoquinoline[7,1], a lyotropic chromonic liquid crystal (LCLC). LCLC thin films cast from concentrated aqua solution (20 % wt.), aligned by shear flow and dried, show strong linear dichroism in their C-, N-, O-, S-*K* edge near edge x-ray spectra (NEXAFS). The carbon *K* edge has been used for quantitative evaluation of the orientational texture of the films at a submicron spatial scale. This has verified there is predominantly in-plane alignment of the LC director. To highlight the role of hydrophobic-hydrophilic interactions, two stereoisomers of the same dye has been synthesized with different positioning of terminal sulfonate groups, in the form of a mixture of isomers with sulfonate groups in 2,10 and 2,11 positions (Y104 compound) and in a 5,10-disulfo arrangement (Y105). Both compounds develop characteristic herringbone-type texture with similar domain sizes. Polarized optical microscopy and higher resolution x-ray microscopy show sinusoidal-like undulations of the molecular director, with occasional crisscross appearance. Such behavior is found to be consistent with earlier observation of striations, characteristic of the columnar phase. The drastic difference in the degree of undulation (±15° in Y104 and ±7° in Y105 films) and long period of undulation (approaching the film thickness) requires further analysis. It was also found that the degree of in-plane order within domains changes from 0.8 for Y104 to >0.9 in Y105 films.

DOI: 10.1103/PhysRevE.76.061703 PACS number(s): 61.30.St, 68.37.Yz, 82.80.Ej, 81.16.Rf

I. INTRODUCTION

The lyotropic chromonic liquid crystals (LCLC) studied in this work represent a special class of lyotropic mesophase which is composed of molecules with a polyaromatic central core and polar hydrophilic ionic groups at the periphery. In a polar solvent (water) the disklike central cores are ordered into a molecular stack with a face-to-face arrangement and the ionic groups are exposed to form a water-aggregate interface [1–4]. A tendency to form such supramolecular aggregates even at low LCLC concentrations make this type of compound a distinct class of LC, whose phase properties are different from their rodlike amphiphilic counterparts. Although there is progress in understanding the basic properties of LCLC [2–4], the nature of the interactions which force the molecules to form supramolecular aggregates is still poorly understood, yet of fundamental importance to unlock the potential of LCLC.

X-ray scattering experiments unambiguously shows that LCLC aggregates have a well defined molecular order with a 0.34 nm separation along the column axis [1–4]. Such packing of aromatic rings has been observed earlier in many orientationally ordered molecular systems, including those of thermotropic (solvent free) compounds [5]. It is attributed to weak van der Waals forces, also referred to as π-π molecular core interactions [6]. On the other hand, experimental data and computer simulations emphasize the role of hydrophobic-hydrophilic interactions [7]. As pointed out by Lydon [1–3], there should be some energy gain as the hydrophobic aromatic rings are stacked adjacent to each other to minimize their exposure to the polar solvent (water), with further screening by peripheral hydrophilic groups [1–4]. From that perspective it is important to measure basic LCLC characteristics as a function of the strength of the solute-solvent interaction. Several approaches are possible, such as variation of ion content or pH, measurement in homologically similar but different strength of solvent, changes in temperature, concentration, etc. [8]. Here we have chosen to use different arrangements of peripheral polar groups on the same polyaromatic framework, the same solvent (water), and the same sample preparation protocol to highlight the role of stereoisomerism of the hydrophilic groups on LCLC aggregate packing.

Current research is also driven by a practical aspect of LCLC compounds, namely, their ability to form thin films with a very high degree of orientational order. This was first noted by Dreyer in 1946 [9]. Recently interest has been renewed since LCLCs provide an inexpensive way to make industrial grade polarizers [10] or to incorporate such films in a liquid crystal display cell as polarizing [11] and compensating films [12], which are especially beneficial when the display is based on flexible plastic rather than rigid glass substrates [13].

Different coating methods using molecular alignment by shear flow, achieved with a rolling applicator rod [14], or by application of an oriented seed layer [15] prior to coating, were explored to establish preferential orientation. It was found that the crystallinity of the dried thin film crucially depends on the degree of orientational order which already existed in the LCLC phase. It also became clear that as the film dries out the system can undergo a phase transition from a nematic phase to a more complex *M*-mesophase

*Konstantine.Kaznatcheev@lightsource.ca

(M=middle), in which the supramolecular assemblies are further ordered in a two dimensional hexagonal structure [16].

Not only the microscopic properties of supramolecular self-assembly, such as mutual ordering of molecules in the column, or column to column orientation, but also macroscopic texture defects, such as disclinations, dislocations, and domain walls, will affect the apparent order parameter and thus the quality of a given LCLC dried film as a polarizer. Although smooth films have been reported for LCLC aligned on buffed polyimide surfaces [15], industrial grade samples show substantial texture. In order to evaluate the role of film texture and to derive a microscopic order parameter we have employed the linear dichroic signal in soft x-ray spectromicroscopy.

Soft x-ray spectromicroscopy [17,18] provides both imaging and spatially resolved near edge x-ray absorption fine structure (NEXAFS) spectroscopy [19]. Over the past two decades, there has been steady improvement in the brightness of synchrotron radiation sources, diffraction optics (Fresnel zone plate), and mechanical aspects of specialized x-ray microscopes. Together, these advances have made scanning x-ray transmission microscopy (STXM) an exceptionally powerful tool for studies of the chemical composition and morphology of soft matter, such as organic and synthetic polymers and composites, emulsions, and liquid mixtures [18]. For most such compounds the NEXAFS spectra yield detailed information on chemical composition at a radiation dose much smaller than that of competitive techniques [20]. The polarization dependence of NEXAFS spectra can be used to determine the orientation of molecules and so yield quantitative information on LC orientational order. Other techniques, such as fluorescence confocal polarizing microscopy [21] and solid state NMR [22], are capable of determining order parameters of LC and have their own merit, but their use requires elaborate sample preparation or synthesis of specifically modified compounds. In contrast, sample preparation is relatively simple for STXM/NEXAFS since it is comparable to "traditional" techniques such as polarized optical microscopy, x-ray diffraction, and conoscopy. Most critically, STXM provides direct insight into LC molecular ordering at a spatial scale not available with other techniques [23,24].

II. EXPERIMENTAL

A. Materials and sample preparation

Sulfonated benzo[de]benzo[4.5]imidazo[2,1-a]isoquinoline[7,1] dye (NBI) was supplied by Optiva, Inc., with two different arrangements of sulfonate terminal groups: as a mixture of two isomers with sulfo groups in 2,10 and 2,11 arrangements, referred here as Y104 dye and in a 5,10-disulfo arrangement referred to as Y105. The molecular structures of Y104 and Y105 dyes are shown in Fig. 1. Both dyes were supplied as 25% (wt.) water solutions and were used without additional purification. Three different sample preparation methods were explored. The first method mimicked the preparation of an industrial film, but used a Si patterned wafer as a substrate. The wafer had a 75-nm-thick

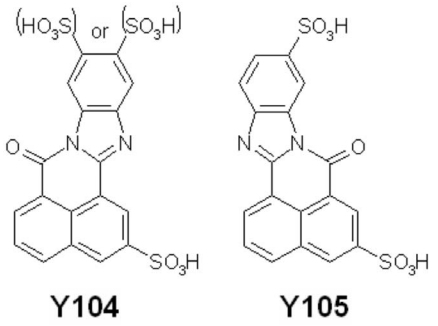

FIG. 1. Molecular structure of Y104 (left) and Y105 (right) dyes. As Y104 compound was supplied as a mixture of two isomers, the alternative attachment of the sulfonate group is shown in brackets.

low stress silicon nitride (Si_3N_4) coating on one side and is lithographically patterned on the opposite side to create 5 mm$\times$5 mm individual chips with a 500 μm$\times$500 μm window etched into the Si substrate to form a Si_3N_4 free standing film which is semitransparent for soft x rays and robust enough to withstand sample manipulation. The complex procedure used to prepare the Si_3N_4 windows in it final steps includes a treatment using a Piranha cleaning solution ($2H_2SO_4+H_2O_2$) to remove any organic residue followed by extensive rinsing with distilled, deionized water and drying in a flow of clean nitrogen. Extended exposure to air tends to leave the wafer surface hydrophobic. To improve surface wettability, the wafer was treated in a plasma (air) etcher just before sample preparation. The dye solution was spread over the whole Si wafer on the Si_3N_4 surface and a wet film applicator rod (Mayer rod with No. 5 wire size) was gently rolled over it creating a shear flow sufficient to align the LCLC molecules. The film was dried out at room temperature in a moderate nitrogen flow. The Si wafer (with etched Si_3N_4 windows) was further split into individual chips to be used in STXM. In the second technique, the industrial grade film deposited on a glass substrate was treated with $BaCl_2$ solution. This results in $Ba^{2+} \leftrightarrow H^+$ ion exchange at the sulfonate group and makes the top layer of the film water resistant. By varying the time of $BaCl_2$ treatment and following water rinsing, it was possible to preserve an unexposed glass to film interface. The film was left in a water bath until it started peeling off the glass substrate. Film flakes were then collected on a standard 400-mesh TEM grid and air dried. In the third method, a small droplet of solution was placed between two Si chips and rubbed until the viscosity increased significantly ("tight feeling"). The chips were then separated and air dried. All samples were examined under a polarized optical microscope (POM). X-ray images at the absorption maximum ($E \sim 285.7$ eV) which highlights film orientational texture, and the corresponding POM images are shown in Fig. 2(a).

POM images show no qualitative difference between samples in which shear flow has been created by rolling of wet applicator rod and samples where shear flow was induced by other means. This further suggests that rubbing or rolling is needed only for initial alignment, and that the final

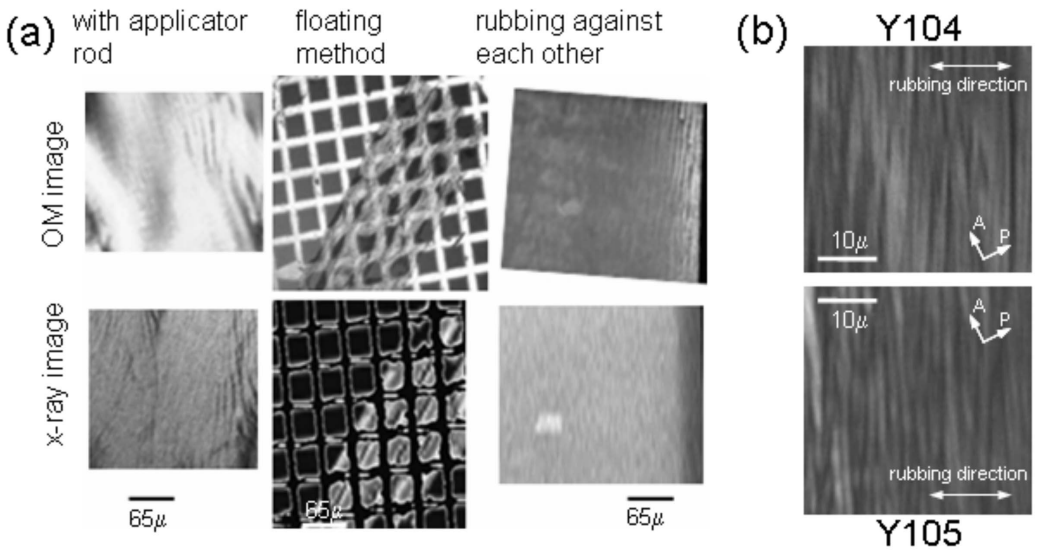

FIG. 2. (a) Polarized optical microscopy (POM) and soft x-ray images (E=285.7 eV) of samples prepared by different techniques (from left to right): spreading over a Si wafer with applicator rod and drying; from "industrial grade" film, followed by Ba fixation and lift off process; rubbing of LCLC droplet between two Si_3N_4 chips and drying out in N_2 flow. All images are cropped to a similar field of view. (b) Magnified POM images of Y104 (top) and Y105 (bottom) thin dried films, prepared by the chip-to-chip rubbing procedure. Rubbing (shear) direction is approximately along the horizontal axis. The cross polarizers were positioned at 45° to vertical/horizontal directions to highlight the presence of herringbone-type orientational texture.

texture is characteristic of the internal LC structure. The observed "herringbone" patterns are similar to those found when an industrial grade polarizer is deposited on a polyethylene film or a glass substrate. All sample preparation methods result in LCLC films with similar texture. The first method tended to produce a lot of broken Si_3N_4 windows, even with moderate force applied to a rolling rod, and left window debris. The second method resulted in some uncertainty as to the rolling direction since floated flecks were collected. The third, which permitted good control over sample thickness and film uniformity, was found to be the best, and was the default method used. The following sections describe results based on measurements performed on the Si_3N_4-Si_3N_4 rubbed chips. No notable differences are found for the Y104 and Y105 samples [Fig. 2(b)]. POM textures are dominated by stripes (which appear as white and black strips), although not so regularly spaced, and with some criss-cross evident. For both dyes, the elongated domains are ordered perpendicular to the shear direction.

Although Y104/105 compounds are novel dyes, they belong to a family of LCLC materials developed earlier. In fact, Violet 20 (2,5-disulfonic acid diammonium salt-peryleno [3″,4″:3,4,5; 10″,9″:3′,4′,5′] dipyridino [1,2-*a*:1′,2′-*a*] bisbenzimidazol-6,11-diol) efficiently doubles the basic structural element of Y104/105 by fusing two units and forming a central perylene core [15]. Although the LC properties might crucially depend on the aspect ratio of the molecule, some relationship of Y104/105 to the "parent" compounds is expected. At room temperature Violet 20 aqua solutions remain in the isotropic state for concentrations below 5% (wt.), nematic order was observed in the 7 to 10% (wt.) concentration range, and M phase ordering was found at elevated concentrations. As for all LCLC compounds, Violet 20 shows pronounced x-ray diffraction peak corresponding to a 0.34 nm molecule-to-molecule packing, negative birefringence, and aggregate formation even at low dye concentration [25,26]. Thin films dried from the N phase show characteristic Schlieren texture, whereas the texture for films formed from the M phase has a more patchlike appearance [27]. Layer-by-layer examination of LC molecule packing reveals that the optical absorption anisotropy increases from an almost uniform layer at the bottom close to the substrate, to highly uniaxial only a few layers (<10 nm) above the substrate [28]. Although the alignment near the substrate likely depends on the type of substrate, its treatment, and the deposition technique, it is clear that the bulk of the sample (to which STXM measurements are sensitive) tends to have a high in-plane anisotropy. This was further confirmed by visible light transmission measurements, which indicate that 100–500 nm thick dried films have strong in-plane absorption dichroism.

Measurement with light oriented along and perpendicular to the shear (rubbing) direction confirmed that the molecular planes are perpendicular to the shear (rubbing) direction on average. Preservation of molecular ordering during drying was studied by Optiva, Inc. [29]. The in-plane order parameter derived from visible light transmission measurements was found to increase from ~0.65 for preoriented, as-deposited LCLC coating to 0.90 after drying, with only small variations due to the sample preparation procedure. It was also noted that casting the film from an isotropic liquid state produced no measurable anisotropy. Atomic force microscopy (AFM) measurements of aggregates confirmed their alignment along the shear direction, likely due to viscoelastic properties of the shear flow [26,28]. Aggregates have a slender cylinderlike shape about the size of the molecule and are

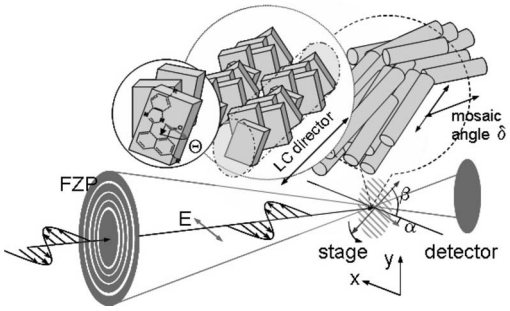

FIG. 3. Schematic layout of experimental settings. Monochromatized x-ray light is coming from the left and focused by Fresnel zone plate to a 50 nm spot on the sample. Transmitted x rays are detected by conversion to visible light by a phosphor and single event detection by a fast photomultiplier. The detection geometry is such that the full radiation cone is measured. The dried liquid crystal thin film is oriented along the shear direction (shown at β to horizontal plane). The characteristic herringbone texture is shown as shaded lines. The three top cartoons depict the molecular arrangements and their relative geometry. Individual molecules (shown as plates) with face-to-face alignment form columns (shown as cylinders). Supramolecular alignment creates bundles. Angular misalignment of one patch relative to another (with characteristic mosaic angle δ) leads to the herringbone texture appearance, seen in POM microscope as black-and-white stripes. The liquid crystal director, a vector along which molecules are aligned on average, is pointed along the long axis of the column. In-plane (azimuthal) rotation of the sample leads to variation of the angle between the E vector of the linear polarized x-rays and the normal to the molecular planes normal angle.

40 to 300 nm long for films cast from an 8 wt. % solution with nematic ordering. Aggregates tend to be bundled, although the relative order was hard to measure. Molecular packing within supramolecules was rather dense as deduced from the small difference between the densities of molecular aggregates in solution and the solid dried dye, as well as the presence of common diffraction peaks in the x-ray scattering data. It was found that M mesophase aggregates form hexagonal packing and the column-to-column separation decreases as the concentration of the dye increases, almost approaching the molecular diameter in the dry film [29]. The aggregates were not only densely packed but also well oriented with maximum crystalline misalignment of 10°–25°.

B. Measurement procedures

Scanning transmission x-ray microscopy (STXM)

An extended spectroscopic analysis was performed at the newly constructed spectromicroscopy (SM) beamline at the Canadian Light Source (CLS) [30]. The beamline energy range of 250–2500 eV permits sulfur K edge spectroscopy and variation of x-ray light polarization. The energy resolution exceeds 5000. Energy calibration was established by measurements of the absorption spectra of gases (C $1s \rightarrow 3p$ in CO_2 at 294.96 eV [31]; N $1s \rightarrow \pi^*$ $(v=1)$ transition in N_2 at 401.1 eV [31]; O $1s \rightarrow \pi^*$ transition (main peak) in O_2 at 530.75 eV [32]; S $1s \rightarrow t_u$ in SF_6 at 2485.9 eV [33]). Soft x-ray images were also recorded at the polymer STXM at the Advanced Light Source (ALS) bend magnet beamline 5.3.2 [34], but to keep image acquisition speed high, lower energy resolution ($E/dE \sim 2000$) was set. A detailed description of the ALS 5.3.2 STXM can be found in Ref. [35]. Figure 3 depicts a schematic of the sample layout. Monochromatized light is focused by a Fresnel zone plate to a ~50 nm in diameter spot and images are generated by monitoring the photon flux transmitted through a thin section of the specimen at fixed photon energy while the sample is raster scanned at the focus. For the 5.3.2 beamline the source is a bend magnet for which the measured linear polarization is 80±5% [36] in the horizontal plane (in the notation of Fig. 3 this corresponds to $\alpha=0$). The sample is placed on an azimuthal rotary stage [37] perpendicular to the incoming light. Azimuthal rotation of the sample leads to a variation of angle between x-ray light polarization and sample shear direction ($\alpha+\beta$), which for ideal molecular ordering coincides with Θ, the angle between the molecular planes and the polarization vector of the light. At the Canadian Light Source, the elliptically polarizing undulator [38] permits an arbitrary inclination of the linear polarization direction, so the light polarization variation, rather than in-plane sample rotation was used to change the angle between the x-ray polarization and the shear direction. In the LC thin film, on average, the molecules (shown as rectangular in Fig. 3) are oriented perpendicular to the substrate ("on-edge" geometry) and the molecular planes are perpendicular to the shear direction, indicated as angle β with respect to the horizontal plane. Similar to a stack of coins, the molecules form columns, with the column long edges along a common direction. In the M phase studied here, supramolecules are known to form a hexagonal lattice, but such details are omitted in the cartoon not only to simplify the picture, but also since these STXM measurements do not provide direct evidence of supramolecular ordering and a detailed study of the internal structure of columnar aggregates falls beyond the scope of this article. Instead, columns are shown to form bundles with a characteristic mosaic angle (δ) between bundles forming the orientational texture of the sample.

The transmission images measured by STXM are converted to optical density images $OD=-\ln(I/I_o)$, using the incident flux signal (I_o) measured at a location on the substrate where LC is not present. Spectra can be measured by locating the beam at a spot of interest on the sample while scanning the photon energy. Full spatial and spectral information is obtained by recording a sequence of images over a range of photon energies of interest. For a sample with few components and known reference spectra, quantitative maps of each component can be derived through regression analysis [39]. By measuring such image sequences in the same region as the sample (polarization) is rotated over a series of angles, the spatial variation of the linear dichroism can be mapped and inverted to deduce the orientation and degree of molecular alignment [37].

III. RESULT AND DISCUSSION

A. NEXAFS spectroscopy of Y104 and Y105 dyes

Features in K edge NEXAFS spectra are commonly described as one electron transitions from an occupied $1s$ core

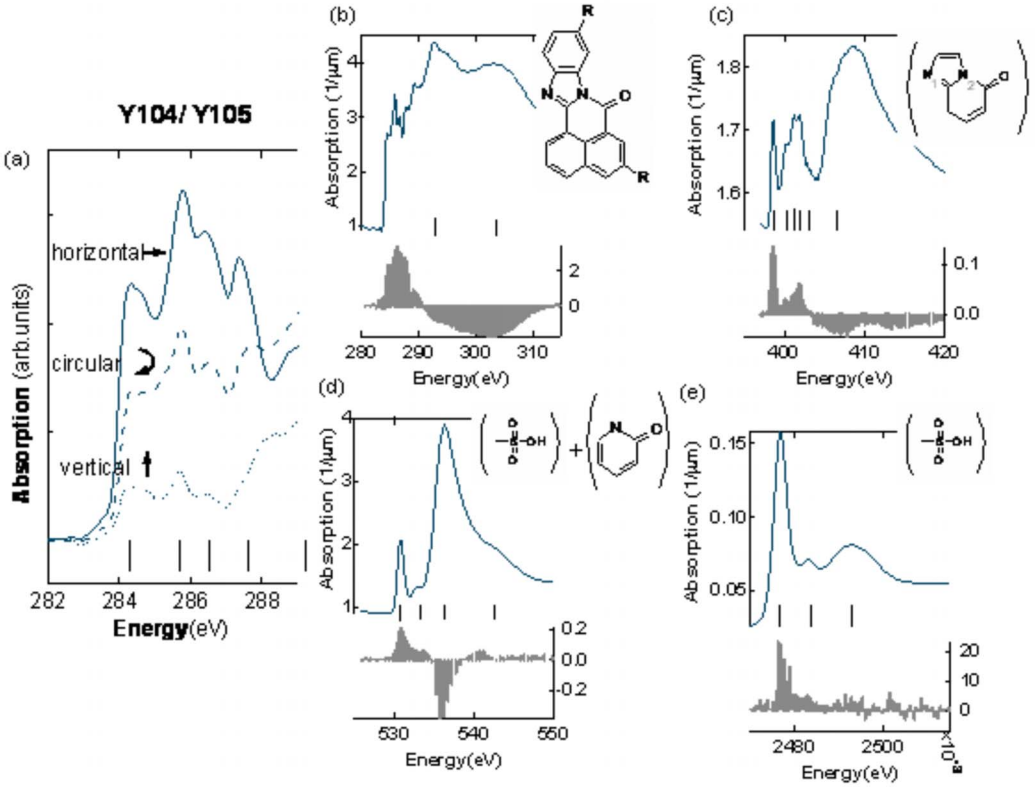

FIG. 4. (Color online) NEXAFS spectra of Y104/ Y105 dyes. (a) Low-energy part of C *K* edge NEXAFS, measured at the same sample location but with three different polarizations of the x-ray light. The solid line corresponds to linear polarized light with the *E* vector horizontal, the dotted line corresponds to linear polarized light with the *E* vector vertical, and the dashed line corresponds to right circularly polarized light. Extended range C (b), N (c), O (d), and S (e) *K* edge NEXAFS spectra (upper panel) and linear dichroic signal (bottom) part are plotted. Short vertical lines mark peaks, whose energy and assignment is given in Table I. Relevant chemical structural elements are shown as inserts. Note the dichroic measurements correspond to in-plane variation of the *E* vector to a shear direction.

level to unoccupied molecular orbitals. NEXAFS spectra of complex molecules often closely resemble the sum of NEXAFS spectra of constituent groups (also referred to as "building blocks"), even in the condensed state [19]. The common moieties are closely linked to chemical functional groups, such as phenyl rings, carbonyl groups, etc., and as such, provide a molecular orbital-based language for NEXAFS spectral interpretation. Although chemical conjugation (orbital delocalization) and symmetry reduction might substantially change spectra, it is often possible to relate particular peaks to individual orbitals of π^* or σ^* symmetry within specific functional groups. In the dipole approximation the peak intensity should vary as $\cos^2(\phi)$, where ϕ is an angle between the electric field vector of the x rays (E) and the direction of the transition dipole moment. For $1s$ (K edge) excitation, the final state symmetry and thus the direction of the transition moment coincides with direction of the unoccupied orbital—i.e., for $1s \rightarrow \pi^*$ transitions, it is along the π^* direction, while for $1s \rightarrow \sigma^*$ transitions it along the σ^*direction which in many cases aligns with a particular bond. In flat aromatic molecules such as the Y104/Y105 dyes, the low energy $1s \rightarrow \pi^*_{\text{ring}}$ transitions should vanish when the x-ray polarization vector (electrical field vector E) lies in the molecular plane and the same transitions should have maximum intensity when the E vector is oriented perpendicular to the plane of the ring [19,40,41] and so the intensity of the corresponding absorption peak should vary as $\cos^2(\Theta)$, where Θ is the angle between the vector normal to the molecular plane and the E vector of the linearly polarized x rays (Fig. 3). As a result, angular resolved NEXAFS determines molecular orientation and soft x-ray linear dichroism can be used in a way similar to other molecular orientation sensitive techniques, such as polarization resolved infrared absorption spectroscopy, x-ray scattering, NMR, or visible light absorption [42].

C-, N-, O-, and S- *K* edge x-ray absorption spectra have been measured at different sample locations on the LCLC films. Examples of these spectra are presented in Fig. 4. It was found that the spectral shape and intensity varies (a) within the sample, (b) at the same sample location on a sample but with different orientation of x-ray polarization vector, and (c) between Y104 and Y105 families. Even so, all spectra consist of peaks located at the same energies, with only intensity variations. This is particularly evident from Fig. 4(a), which shows the low-energy part of the C edge NEXAFS spectrum. To further prove that the observed spectral variation is due to orientational order and the difference in spectra is a linear dichroic signal, we varied the polarization of the incoming light, while keep the spot steady at the same sample position. The intensity of the peak at 284.3 eV,

its prominent shoulder at 284.7 eV, the main peak at 285.7 eV, and the peaks at 286.5 and 287.8 eV all change by approximately the same factor, while keeping their energy position steady. The circularly polarized spectrum falls in between the linear vertical and linear horizontal curves, as expected since linear dichroism disappears with pure circularly polarized light. Even close to the ionization potential (IP) region (289–291 eV), fitting analysis suggests that no new peaks or energy shifts are observed.

The full range of the C 1*s* spectrum is shown in Fig. 4(b), while long range spectra in the N 1*s*, O 1*s* and S 1*s* spectral ranges are presented in Figs. 4(c) and 4(d) with their dichroic signals plotted in the bottom panels of each figure. No distinct spectroscopic difference between Y104 and Y105 dyes was found even over the extended energy range. To emphasize this, cartoons of the molecular moieties common to Y104 and Y105, and related to C-, N-, O-, S- *K* edge transitions are added to Figs. 4(b)–4(d). To quantify the Y104/ Y105 absorption spectra, they have been scaled to a stoichiometrically weighted sum of elemental x-ray absorption data which is known to match the soft x-ray absorption far from the edges [43]. The 250 nm thick films are semitransparent to soft x rays and so STXM is well matched for studies of industrial grade polarizers (films of submicron thickness, depending on the application) and measurements of the orientational properties in the bulk of LCLC phase.

Table I summarizes the peak energies (marked on Fig. 4 as vertical bars at the bottom of each NEXAFS spectra), estimated term values and proposed assignments of the spectral features. In the absence of quantum calculations or complimentary photoelectron data, we have interpreted the spectra using a few approximations. The ionization potentials (IP) are estimated based on the values for small molecules [44], which likely are correct within 0.5 eV. For the C 1*s* edge, the complex π^* structure is mainly determined by core level chemical shifts which are particularly rich in this molecule since carbons adjacent to different types and numbers of heteroatoms [N, O, (NO), SO_2OH] will have characteristic shifts. The first peak at 284.3 eV is at a very low energy relative to other unsaturated organic molecules. This is consistent with the small highest occupied molecular orbital (HOMO), lowest unoccupied molecular orbital (LUMO) gap (giving rise to the bright yellow color of the Y104/ Y105 dyes) and thus low-lying LUMO level. There is a shoulder at about 0.4 eV higher energy. This shifted peak is ascribed to C $1s(\text{C-SO}_2\text{OH}) \rightarrow \pi^*$ transitions. In principle it should be considerably weaker as in a formal treatment there are 11 sites (C or C-H on the rings) contributing to the lowest-energy peak and only two sites contributing to the shoulder. This suggests the spectrum is more complicated and C $1s(\text{C,CH}) \rightarrow \pi^*$ transitions contribute to the low lying band below 285 eV. The most intense of the π^* features is that at 285.7 eV which is assigned to C $1s(\text{C-N}) \rightarrow \pi^*$ transitions. The peak at 0.8 eV higher energy is attributed to the corresponding excitation at the ring carbon which is bonded to two N atoms. Finally the peak at 287.8 eV corresponds to the C $1s(\text{C}{=}\text{O}) \rightarrow \pi^*_{\text{C}=\text{O}}$ transition, which is close in energy to the peak for C $1s \rightarrow \pi^*_{\text{amide}}$ excitation (288.2 eV) in proteins. The features at higher energy are assigned to various C $1s \rightarrow \sigma^*$ transitions, based on trends in the energies of such transitions with bond type and bond length. In particular the 290–310 eV region is rich in $1s \rightarrow \sigma^*$ transitions as is evident from the change in sign of the dichroic signal.

The N 1*s* spectrum [Fig. 4(c)] also has a complex low-lying π^* structure from 398 to 402 eV, which is associated with the presence of two different N arrangements, one adjacent to the C=O bond (amide), the other to the regular position of N atom in imidazole. Direct transitions from each N site to the LUMO π^* of the ring are attributed to the peaks at 398.6 and 400.2 eV, respectively, they have an estimated term value of 7.4 eV in good agreement with counterpart transitions in the C 1*s* spectrum. From analogy with other amide structures such as proteins, N 1*s* excitation to the level primarily associated with the carbonyl occurs at 401.2 eV, which is the basis for our assignment of the third N 1*s* feature to the N $1s(\text{N-amide}) \rightarrow \pi^*_{\text{C}=\text{O}=\text{amide}}$ transition [45]. The highest energy N $1s \rightarrow \pi^*$ transition at 401.9 eV has a less clear origin; it may be a transition to another delocalized π^* orbital. At higher energies there is strong broad signal with in-plane transition moment which is from various overlapping N $1s \rightarrow \sigma^*_{\text{C-N}}$ transitions.

The O 1*s* spectrum [Fig. 4(d)] has a much simpler π^* structure than the C 1*s* or N 1*s* spectra. As evident from the molecular structure shown as an inset, there are two types of O sites—the carbonyl and the sulfonated oxygens. In the present work, we do not differentiate protonated ($-\text{SO}_2\text{OH}$) and deprotonated ($-\text{SO}_3^-$) states of the sulfonate group. Further analysis of salt solutions or the pH dependence are needed to clarify if this is a critical factor in the NEXAFS spectra of sulfonates. The lowest energy peak is attributed to O $1s(\text{C}{=}\text{O}) \rightarrow \pi^*_{\text{C}=\text{O}}$ excitations. Its energy is somewhat lower than that of other amides (e.g., 532.1 eV in proteins [45]), but this is likely due to partial delocalization through mixing with the ring $\pi^*_{\text{C}=\text{C}}$ orbitals. The second discrete out-of-plane symmetry transition at 533.2 eV is attributed to O $1s(\text{SO}_2\text{OH}) \rightarrow \pi^*_{\text{S}=\text{O}}$ transitions. In general $1s \rightarrow \pi^*$ transitions at unsaturated bonds involving third row elements are significantly weaker than those involving only second row elements. The very intense broad peak at 536.7 eV is attributed to O $1s(\text{SO}_2\text{OH}) \rightarrow \sigma^*_{\text{S}=\text{O}}$ transitions, while the broad signal around 543 eV is assigned to O $1s(\text{C}{=}\text{O}) \rightarrow \sigma^*_{\text{C}=\text{O}}$ excitations.

The S 1*s* spectrum is shown in Fig. 4(e). All features have mainly out-of-plane character. We attribute the sharp lowest energy peak to S $1s \rightarrow \pi^*_{\text{S}=\text{O}}$ transitions. The weak peak at 2483 eV is attributed to S $1s \rightarrow \sigma^*_{\text{S-C}}$ transitions while the stronger broad peak at 2493 eV is attributed to S $1s \rightarrow \sigma^*_{\text{S}=\text{O}}$ transitions. With a view to using these spectra in the future to chemically identify sulfonated dyes in mixtures with nonsulfonated materials, we note that the spectral features characteristic of the sulfonated group are the strong peak at ~537 eV in the O 1*s* spectrum and the sharp peak at ~2477 eV in the S 1*s* spectrum.

B. Orientational maps

Based on the spectroscopic assignment of the peaks, the orientational texture, i.e., the intensity variation due to the

TABLE I. Absolute energies, term values, and proposed assignments for NEXAFS features in the C 1*s*, N 1*s*, O 1*s*, and S 1*s* spectra of Y104/Y105 dyes.

Carbon 1*s*	Term value (eV)					Assignment				
Energy (eV)	CH	C—SO_{3H}	CN	CN_2	C=O	CH	C—R	C—N	CN_2	C=O
284.3	6.0					$1\pi^*$				
284.7		6.3					π^*			
285.7			6.5					$\pi^*_{C=N}$		
286.5				6.5		$2\pi^*$			$\pi^*_{C=N}$	
287.8					7.5	σ^*_{CH}				$\pi^*_{C=O}$
289.2							σ^*_{C-S}			
290.3	IP									
291		IP								
292.8						σ^*_{C-C}				
292			IP							
293				IP						
294.3 (sh)								σ^*_{C-N}		
295					IP					
296.3 (br)						σ^*_{C-C}			σ^*_{C-N}	
303 (1)										$\sigma^*_{C=O}$

Nitrogen 1*s*	Term value (eV)		Assignment (final orbital)	
Energy (eV)	C=N	N-amide	C=N	N-amide
398.6	7.4		$\pi^*_{C=N}$	
400.2		7.3		$\pi^*_{C=N}$
401.2		6.3		$\pi^*_{C=O(amide)}$
401.9	4.1		$\pi^*_{C=C}$	
406.0	IP			
406.1 (sh)	−0.1		$\sigma^*_{X=N}$	
407.5		IP		
408.6(3)		−1.1		$\sigma^*_{X=N}$
420(2)	−14	−13	$\sigma^*_{X=N}$	$\sigma^*_{X=N}$

Oxygen 1*s*	Term value (eV)		Assignment (final orbital)	
Energy (eV)	C=O	SO_3H	C=O	SO_3H
530.8	7.2		$\pi^*_{C=O}$	
533.2		7.8		π^*_{SO}
536.7 (STRONG)		3.3		σ^*_{SO}
538	IP			
541		IP		
543(1)(sh)	−5		$\sigma^*_{C=O}$	

Sulfur 1*s*V)	Term value (eV)	Assignment (final orbital)
Energy (eV)	SO_3H	SO_3H
2476.8	7.0	$\pi^*_{S=O}$
2483.0	0.8	σ^*_{S-C}
2483.8	IP	
2493.0(5)	−10	σ^*_{S-O}

difference in molecular alignment otherwise chemically homogeneous and uniform specimen, will be maximum at the C $1s \rightarrow \pi^*$ transitions (284–288 eV). The contrast between two molecular patches might also vary as a function of the angle between the light polarization and the average molecule plane orientation. Numerical analysis suggests that two adjacent domains with a splay of ~10° in the in-plane molecular director, should have maximum intensity if the light polarization vector is inclined to the in-plane director at a ~50° angle. Figure 5(a) shows x-ray images measured at

285.7 eV and converted to OD of Y104 (top) and Y105 (bottom) films rotated by ~45° (the direction of the shear flow is indicated at each image by the bidirectional arrow). These images clearly show a herringbone-type texture, consisting of alternating black and white stripes (orientational contrast modulation), with criss-cross striations, especially prominent in the Y105 sample [Fig. 5(a) lower panel]. For both Y105 and Y104 samples, the texture looks similar, consisting of ~15 μm × 1.5 μm domains elongated perpendicular to the shear (rubbing) direction. Further, with accurate azimuthal rotational stage calibration (to account for off-axis shift) and cross-correlation of sample location to markers, it was possible to measure the NEXAFS spectral variation as a function of sample rotation within the same domain, at the locations indicated by the dots in Fig. 5(a). The results are shown in Fig. 5(b), with the top spectra corresponding to the Y104 film, and the bottom spectra to the Y105 film. An insert of Fig. 5(b) plots the angular variation of the low energy $1s \rightarrow \pi^*$ peaks for both specimens as a function of rotational angle. Similar angular behavior has been observed at other sample locations. For both films, the maximum π^* absorption is found when both the shear direction and the linear polarization vector lie in the horizontal plane, and the minimum absorption occurs when these directions are perpendicular to each other, thus confirming that the molecules on average stay perpendicular to the substrate with the molecular planes aligned perpendicular to the shear direction.

In order to obtain quantitative information about the orientation, we have fit the angular variation of the peak intensity to Eq. (1):

$$I(\beta) = A^* \cos^2(\beta + \delta) + C, \tag{1}$$

where A is the amplitude of modulation, C is a constant, and β is the sample rotation angle. Note that in Fig. 5(b) we omitted δ (in-plane mosaic angle) since there is some ambiguity with its value with the manual in-plane rotation used for 5.3.2 STXM measurements where the sample rotation angle has to be derived from the image rotational alignment. All three low-energy peak intensities closely follow the $\cos^2$ behavior expected for simple dichroic signal variation with minor variation in A and C coefficients. The main difference between the Y104 and Y105 samples is in in the ratio of A (amplitude) to C (baseline constant). In the Y105 dried film the angle variation of the π^* signal is more pronounced and falls closer to zero when the sample is rotated by 90°.

Following a procedure described by Stohr *et al.* [46,47] we determined the average fraction of molecules with their aromatic core planes ordered normal to shear direction [$f_x \sim A/(A+C)$], and the fraction with their aromatic core planes ordered along the shear direction and normal to the surface of the film [$f_y \sim C/(A+C)$]. As the sample mounting is such that it is fixed perpendicular to the incoming x rays the out-of-plane component of the molecular director cannot be measured. Given the unidirectional nature of columnar aggregates confirmed experimentally and the high value of in-plane molecular alignment, it is reasonable to assume that f_z (the fraction of molecules with their core plane parallel to the film surface) is small and equal to f_y. A fit to Eq. (1) of the data plotted in Fig. 5(b), gives values of $A=1.12$, $C=0.25$ for the Y104 film and $A=2.1$, $C=0.15$ for the Y105 film. These values correspond to $f_y=f_z \sim 0.12$, $f_x \sim 0.75$ for Y104 and $f_y=f_z \sim 0.05$, $f_x \sim 0.9$ for Y105 in the region sampled. The optically anisotropic film can be characterized by refractive index tensors (rather than scalar) which to some approximation can be derived from a molecular tensorial order parameter. For nematic films, it is common to present the order parameter tensor in its diagonal form with just two scalar order parameters S: the uniaxial order along the major nematic axis and P: the molecular order anisotropy in the plane perpendicular to the nematic director. We follow this formal treatment and extend it to the columnar phase, where S will be the in-plane molecular order of the film along the shear (rubbing) direction. In this case the derived order parameters are $S=1/(2-3f_x)$ and $P=3/2(f_z-f_y)$ [48]. The case of $S=1$, $P=0$ corresponds to a perfectly aligned molecular system with molecular planes lying perpendicular to the shear (rubbing) direction. For $S=-1/2$, the molecular planes are aligned along the shear direction, and P can vary from 0, if the molecules are randomly oriented perpendicular to the film surface direction (no biaxiality should be measured), to 3/2 if all molecular planes are aligned perpendicular to the film surface normal (the so-named, "flat-lying" case where

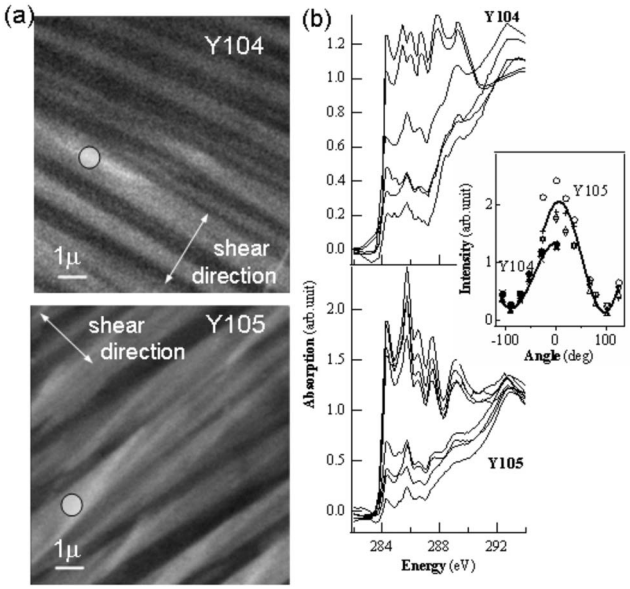

FIG. 5. Spectral angular variation within the domain. The top panel refers to Y104 while the bottom panel refers to Y105. (a) OD images (at 285.7 eV) of Y104/ Y105 sample taken at approximately 45° sample rotation. Rubbing direction is shown as the bidirectional arrow. Light spots indicate the location where NEXAFS spectra (shown at the right) are extracted. Note that the actual size of the x-ray beam is only 50 nm, but the data have been averaged over the larger area indicated to account for possible sample misalignment. (b) Low energy C edge NEXAFS spectra variation for different sample rotations. The sample OD at high energy is normalized to unity. The insert plots the variation of the peak intensity as a function of the sample rotation angle. Open markers correspond to Y105 film, dashed to Y104 sample, individual energy intensity are 284.3 eV as crosses, 285.6 eV as circles, 286.5 eV as tip up triangles, 287.7 eV as tip down triangles, solid lines are the fit to $\cos^2$ function with parameters as described in the text.

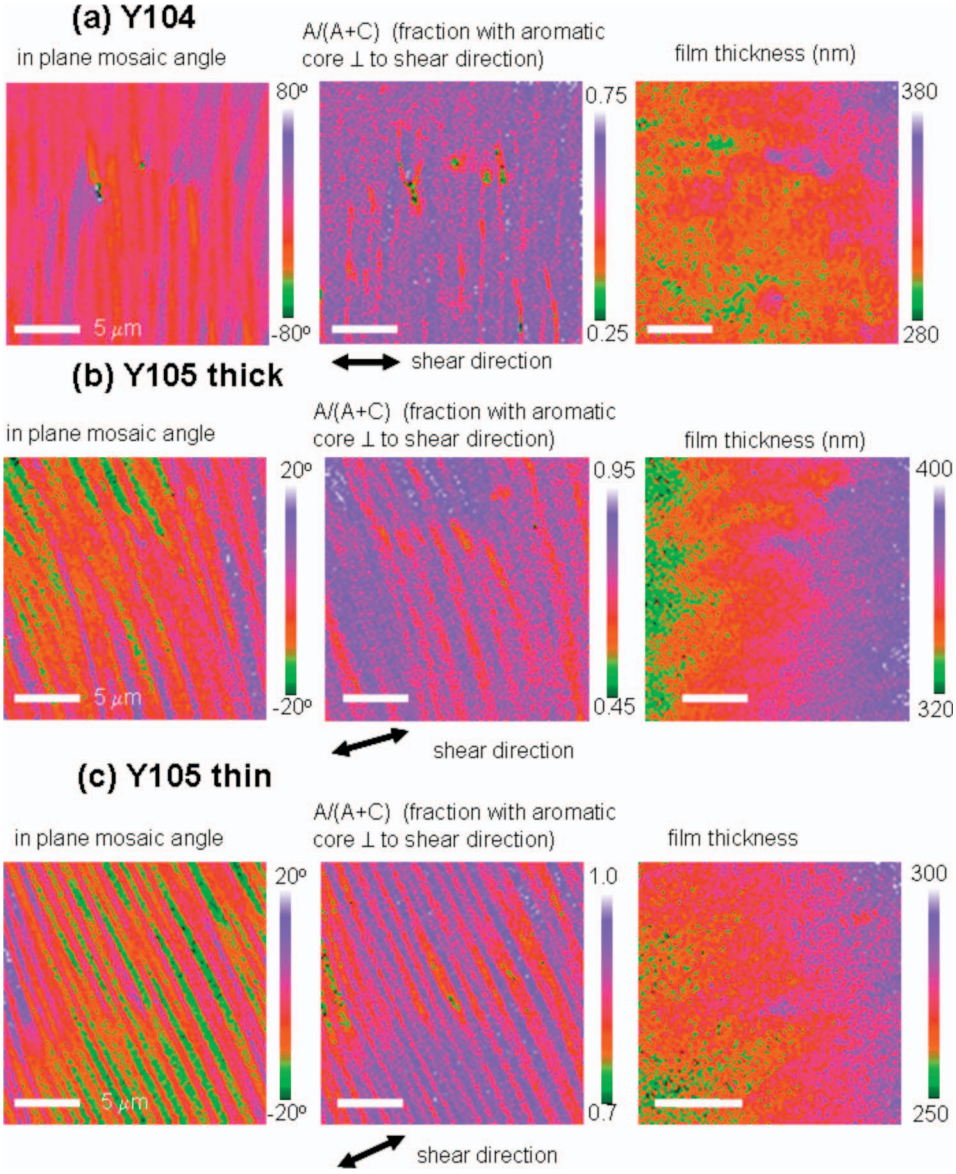

FIG. 6. (Color) False color image of crystalline film orientational texture, as green (with minimum value as indicated on the color bar) to violet (maximum) color palette: (a) Y104, (b) Y105 thick, and (c) Y105 thin films. For each row, the left panel shows maps of the in-plane mosaic angle (the angle between shear direction and local in-plane LCLC director) map, the middle panel shows maps of the magnitude of in-plane director defined here as a fraction of the molecules with their aromatic core plane oriented normal to the local in-plane director, and the right panel shows maps of the sample thickness, as deduced from x-ray absorption intensity in the C 1*s* continuum. All images in a given row are rescaled to the same region of interest. White bars show the spatial scale while the shear direction is marked by double sided black arrows below the images.

the $1s \rightarrow \pi^*$ transitions should not be visible in the STXM geometry). Numerical estimates suggest $S=0.8$ for Y104 and $S>0.9$ for Y105 films, although these values are likely underestimated due to the finite ellipticity of the otherwise linearly polarized light in the ALS 5.3.2 bend magnet beam line [36,49].

The measurements of the angular variation of the π^*-peak intensity can be further extended to image acquisition with pixel by pixel fitting to the $\cos^2$ function. Such measurements have been performed at the CLS STXM, where the polarization direction of the linear polarized light can be rotated in the plane of the sample by changing the phase of the elliptically polarizing undulator (EPU). As the sample position remains fixed, the quality of data analysis is dramatically improved, so one can fit the angular variation of the absorption intensity at each (i,j) pixel to a function $A_{ij}\cos^2(\alpha-\delta_{ij})+C_{ij}$ [37], where $A_{ij}/(A_{ij}+C_{ij})$ is a measure of the fraction of molecules with vector normal to molecular planes aligned at an angle δ_{ij} to the shear (rubbing) direction, and $C_{ij}/(A_{ij}+C_{ij})$ corresponds to the fraction of molecules with their molecular plane aligned along x-ray light polarization direction. Finite x-ray light ellipticity and second order contamination might still contribute to an "artificially enhanced value" of $\langle C_{ij}\rangle$ and so a reduction of "apparent" order. Measurements to date indicate the light polarization purity is better that 95% linear [38]. To improve the statistics of this analysis, the most intense C $1s \rightarrow \pi^*$ transition at 285.7 eV was used.

The result of these dichroic measurements performed on a new set of samples is shown in Figs. 6(a)–6(c). In each figure, the left image corresponds to the mosaic angle variation while the middle corresponds to molecular order, presented here as the fraction of molecules with their molecular plane aligned perpendicular to the columnar direction. The third row plots the sample thickness, as deduced from the x-ray absorption signal at energy above the C *K* edge. To highlight the correlation of the orientational texture with sample thickness, two different areas [Fig. 6(b) for thick and Fig. 6(c) for thin] of the same dry film (Y105) have been presented. All images are scaled so that the intensity variation of each color

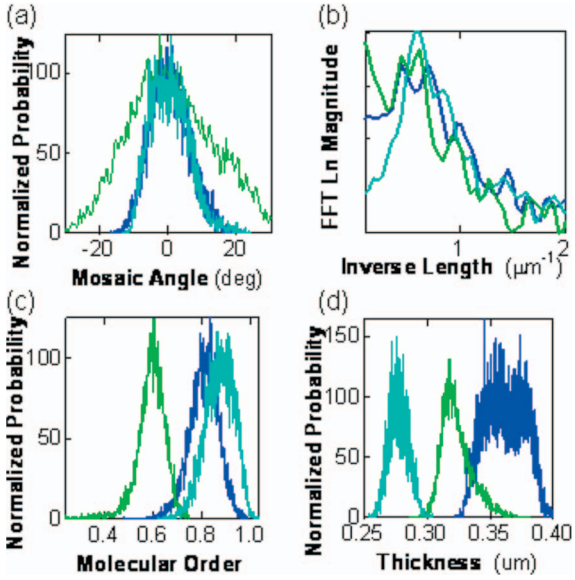

FIG. 7. (Color) (a) Mosaic angle distribution function derived from histograms of the images shown in Figs. 6(a)–6(c) first column. (b) Magnitude of Fourier transformation (logarithmic scale) of mosaic angle images [Figs. 6(a)–6(c)] averaged along direction perpendicular to shear and plotted as inverse length function (linear scale from 0.1 to 2 μ^{-1} to highlight characteristic length of in-plane undulations). (c) Normalized histogram of the in-plane molecular order distribution for Y104, Y105 thick, and Y105 thin films derived from Figs. 6(a)–6(c) middle column. (d) Film thickness variation as deduced from Figs. 6(a)–6(c) right column. For all figures, green curves correspond to Y104 film, dark blue lines to Y105 thick region, and light blue lines to thin section of Y105 film.

maps to the full range of the corresponding parameter. A red-green-blue color palette is used for these maps with maximum and minimum values as indicated by color bars next to each image. Histograms of mosaic angle variation (a), its Fourier transform to determine the characteristic length (b), the in-plane molecular order variation, defined as the fraction of molecules with their aromatic core plane aligned perpendicular to the in-plane LC director (c) and film thickness (d) are presented in Fig. 7 with the data for the two different samples plotted on the same scale to facilitate comparison.

C. Origin of the texture

In-plane striation develops after the deposition of the film and during its drying. The detailed mechanism of formation is not known and might involve both static and flow-induced phenomena. In-plane striations are often observed in a system similar to lyotropic chromonic liquid crystals, namely, in the columnar phase of thermotropic compounds. In fact, the appearance of striations perpendicular to the column direction were carefully studied by temperature induced dilation and attributed to thin film thermomechanical instabilities [50]. The interpretation is similar to that for the Helfrich-Hurault undulation instability in smectic (layered) liquid crystals as described by de Gennes and Prost [51]. The physical mechanism is the following. Imagine a layer of parallel and straight columns filling a space between two fixed walls; with the columns parallel to the confining walls. Suppose that the thickness of each column (or the separation between the adjacent columns) decreases, say, as a result of thermally induced contraction or as a result of water evaporation, as in our case. If the overall sample size (the distance between the walls) is fixed, then the system finds itself under a stress; it needs to fill the same space but with "thinner" columns. The system can relax the stress by either creating more columns or by tilting the columns with respect to the walls (the effective thickness of the tilted column measured along the normal to the wall is higher than the thickness of the column measured along the normal to the column). Creating new columns requires nucleation of dislocations and their propagation through the entire system; generally, this is a very slow process [52]. Tilt of the columns, on the other hand, does not require any nucleation and occurs quickly, especially if it is periodic with alternating directions of the tilt. The periodic tilt is also preferred over the uniform tilt because the columns on average remain parallel to the confining walls.

The simple geometry above can be applied to the in-plane undulations of columns and to the undulations in the vertical plane, as these two are decoupled [50]. However, since the typical dimension of the samples in the plane of the film is much larger than the thickness of the film, the undulation instability occurs first in the horizontal plane [52]. By assuming that the columns remain parallel to both top and bottom surfaces of the film and by balancing the stress energy associated with the changing distance between the columns and the curvature energy associated with curvature of columns (accommodating their periodic tilt), one can find the threshold stress γ_c and the periodicity of undulations in the plane of the film [50,52]:

$$\gamma_c = \frac{\pi\lambda\sqrt{A}}{d(1-A)}, \quad \Lambda_c = 2\sqrt{\pi\lambda d}/\sqrt[4]{A}, \tag{2}$$

where $\lambda = \sqrt{K/B}$ is a penetration length, K is the curvature elastic constant, and B is the compressibility modulus; d is the sample thickness and A is the elastic anisotropy equal to $(B_u - B_v)/(B_u + B_v)$, where B is the compression modulus, u the direction perpendicular to the film surface, and v the in-plane of the film, perpendicular to average direction of the columns. Immediately above the threshold, $\gamma \geq \gamma_c$ the undulations are sinusoidal with a period that depends on the film thickness $\Lambda_c \propto \sqrt{d}$ (notations are the same as those of Oswald [50]).

Note that the threshold stress γ_c is very small and determined by the ratio of an essentially molecular length scale λ (which should be of the order of the intercolumnar distances, i.e., a few nm) to the macroscopic thickness d of the film $\lambda/d \sim 10^{-2} - 10^{-3}$. Therefore, an undulation can be caused by a very small decrease in the intercolumnar spacing associated with only a few percent of composition change caused by water evaporation. At higher stresses, one expects a transformation of the sinusoidal profile into a sawtooth (or sharp zigzag) profile [50] and such a transformation is indeed observed experimentally in smectic materials [51]. For the saw-

tooth undulations, the nonlinear model (valid above the threshold) predicts that the undulation period changes very little with the stress but the "mosaic" angle increases monotonically

$$\Lambda \approx 1.05\Lambda_{vc}, \quad \delta \approx 2\sqrt{\gamma}. \tag{3}$$

Some points should be addressed before further comparing the experimental data with this theoretical framework. First, the texture we observed is in a dried film, rather than as a result of temperature variation in a liquid film near equilibrium. Although the critical dilation might happen as a result of rapid LCLC phase precipitation, even if the overall film thickness shrinks as the film dries, column buckling will also occur for in-plane compressed films [53]. The source of compression along the column axis might be the continuous growth of the supramolecules expected as LC relative concentration increases. It might also occur as a result of fluid instability forced by shear flow, as this is known to induce column alignment. In the experiment we have performed, the initial stage of film preparation is poorly controlled and the film starts to dry out during the time it is spread, so we can not confidently record initial steps of texture appearance and conclude if it is quenched by film drying or proceeds throughout. Even if the origin of the instability of the drying LCLC film might be unclear, it is important to note that different sample preparation methods, substrates used, or different LCLC dyes [54] all result in a remarkably similar texture. Thus we believe the observed texture is characteristic of the intrinsic properties of the LCLC dye rather than being a function of the sample preparation procedure.

According to the model of Ostwald *et al.* [50], the in-plane undulation period should be proportional to the square root of film thickness. Neither domain size variation within the same film, nor period variation between different films cast from the same dye solution show clear square root dependence expected, as one can see from Fourier analysis of the film modulation shown in Fig. 7(b). Although it might be that film defects obscure an expected 15% difference in a period of modulation for thick versus thin Y105 films, the remarkable similarity between the Y104 and Y105 films [see also Fig. 5(a)] is less expected. The discrepancy between the experimental data and model predictions is especially clear when one considers the numerical data for the undulation periodicity. Following estimates given by Oswald [50], the numerical value of λ is expected to be close to intercolumnar distance, i.e., about a few nanometers. The thickness of the dry film is less than 0.5 micron. Therefore, the period of undulations, $\Lambda_c \propto \sqrt{\lambda d}$ is expected to be submicron, certainly smaller than the film thickness. This is not the case in our experiments, as the period is clearly in the range of a few micrometers as evident from Figs. 5–7. Even if one assumes that the undulations develop at the stage of the "wet" film of thickness in the range of $\sim$1–2 μm, the discrepancy is still serious.

There are a few factors that might be responsible for these discrepancies. In the model [50], one assumes that the columns adjacent to the surfaces of the sample remain strictly straight and parallel even at high stresses. This might not be the case, as (i) the surface anchoring forces are always finite [53,55] and (ii) the orientation of columns at the top and bottom interfaces might not be the same (hybrid alignment). Below we discuss both factors.

Finite (as opposed to infinitely strong) surface anchoring facilitates undulations, as demonstrated for the case of smectic undulations [53,55] and might explain the numerical discrepancies above. The period of undulations in weakly anchored smectic cells increases with stress rather dramatically, by about 50% [53,55] which is noticeably larger than the increase by 5% predicted by the infinite-anchoring model of columnar undulations [50].

Hybrid alignment of columns at the opposite interfaces creates elastic distortions in the vertical plane of the film. As water evaporates and the thickness of the film decreases, these distortions increase. At some threshold, the vertical distortions might be relaxed by in-plane periodic deformations, as demonstrated for thin (submicron) nematic films of thermotropic compounds [56]. The observed period of distortions in hybrid aligned films is typically much larger than the films thickness [56] which makes it closer to the experimental situation at hand as compared to the undulation mechanism. However, further comparison is difficult as we have no direct measurement of surface orientation of the columns. Finally, let us mention that other surface effects might need to be taken into account when one of the surfaces is free, just as capillary waves account for spinoidal decomposition of thin binary films.

D. Comparison of the Y104/ Y105 films

As evident from the Fig. 7(a) histograms, both films show close to Gaussian mosaic angle distributions. The absence of any two peak structure characteristic of zigzag formation, suggest that all films texture are formed at $\gamma \sim \gamma_c$ (and likely to be quenched at such stage by film drying). The main difference between the Y104 and Y105 films appearance is the characteristic value of mosaic angle. In the Y104 dried film it FWHM is 30°, whereas for Y105 it is only half of that. Following Eq. (3), we may conclude that Y104 films are developed under a higher stress. By combining with Eq. (3) $\frac{\delta_{Y104}}{\delta_{Y105}} = \sqrt{\frac{A_{Y104}}{A_{Y105}}}$, there should be a remarkable difference in the elastic anisotropy constant for Y104 and Y105 compounds. In the following we discuss its molecular origin.

Y104 and Y105 molecules are primarily different due to sterioisometric arrangements of the sulfonate groups placed at the different ends of the central aromatic core. In solution they are negatively charged (SO_3^-) and so lead to anisotropic behavior within the molecule. The carbonyl group is also expected to be more negatively charged compared to the positively charged amino bridge [15], and as such, the *cis* arrangement of the carbonyl and sulfonate groups (Y105) is expected to be less anisotropic than the *trans* arrangement (Y104). Although the experimentally observed differences in amplitude of in-plane undulation seems to be in qualitative agreement with expectations from these molecular structural differences, some questions remain. For instance, substantial anisotropy along the major axis of the sulfonate groups (anisotropy within the molecule) should be accompanied by a coaxial arrangement of adjacent molecules (to keep aniso-

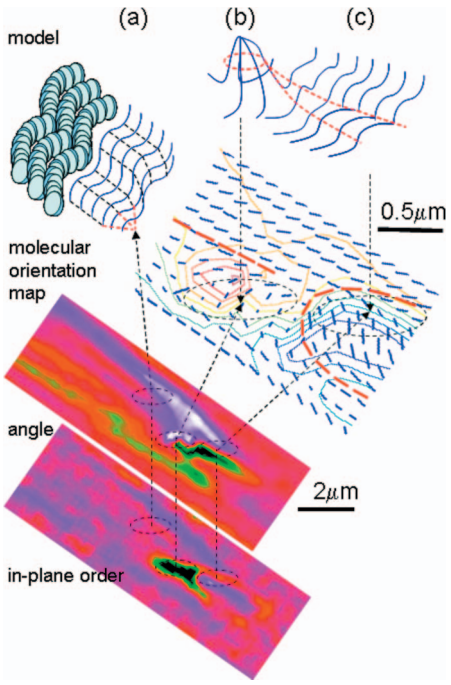

FIG. 8. (Color) LCLC film characteristic defects. The color coded images (called "molecular orientation maps") of in-plane angular orientation of LC director (labeled "angle") and the magnitude of order parameter (labeled "in-plane order") are taken from Fig. 6(a), but truncated to the region of interest, zoomed, rotated by ~120° and aligned on top of each other. Those two images have been combined and plotted as a vector field image, where the length of the bars (plotted in blue) are proportional to the magnitude of the order parameter and the bar orientation is given by the LC director angle (chosen here such that bars oriented perpendicular to the in-plane director indicate the aromatic core molecular plane). This image provides a convenient visualization of molecular alignment, as it displays the molecular arrangement if viewed from above the film. Red bars are a hand sketch of molecular alignment expected in the vicinity of a $\frac{1}{2}$ disclination and are only for eye guidance. Thin black dashed lines are the pointers to link the same regions on all maps and cartoons. We also chose to display the angular map as color coded contours superimposed on the "molecular orientation map." Cartoons (labeled as "model") placed at the top and sides of the figure show the molecular arrangement associated with each type of defect. Contrary to the bar representation of the molecular alignment, these are drawn as continuous lines resembling molecular columns which permits a 3D representation of the molecular ordering. Model (a) shows in-plane undulation characteristic of LCLC *M* phase texture with in-plane conical narrowing of undulation period. Molecules (shown as elongated ellipses) ordering along the individual column are drawn on the left; the expected hexagonal packing is omitted. (b) and (c) are models showing column alignment in the vicinity of a $\frac{1}{2}$ disclination, where the columns are rotated in the direction toward the film surface in the form of a dome with an extended wedge on one side.

tropy between the molecules). In such an arrangement, one expects molecule to molecule electrostatic repulsion due to the similarly charged end groups, unless it is well screened by a water network. The degree of intermolecular ordering should depend on the extent of such charge screening. Does lower molecular order evident for Y104 films [Fig. 7(c)] always correlate with higher degrees of in-plane undulations? Such questions need further analysis and development of a more detailed model. These results indicate that molecules within the column not only have a face-to-face arrangement but also retain some in-plane rotational order despite thermal motion. Molecular anisotropy should also be sufficiently strong to yield desirable elastic constant differences, as hexagonal column packing, reported for *M* mesophase, will further lower the bulk anisotropy.

E. Defects in Y104/Y105 films

Close examination of Fig. 5(a) suggests that, in additional to the sinusoidal-like undulation which results in striations perpendicular to the shear direction, there are conical structures with a characteristic scissorlike appearance. Figure 8 gives an expanded view of one such region in the Y104 film. In the lower image the color variation is proportional to in-plane order; in the middle image the color variation corresponds to LC director angular variation; while a cartoon of characteristic defects deduced from those two images is given at the top of Fig. 8. Three different defects are shown: (a) conical-like inclination, (b) fast angular variation collapsed into a point, and (c) an adjacent wedgelike domain boundary.

The molecular map, derived from the angle and magnitude of in-plane director field, shows that (b) and (c) defects are linked to each other and are the evolution of a $\frac{1}{2}$ disclination characteristic to nematic phase Schlieren texture. Since a walk around a $\frac{1}{2}$ disclination leads to a 180° flip of molecular orientation, only one wing of the disclination can be continuously merged with the underlying in-plane undulating texture, while the other side is forced to be wedged into existed undulations and create a domain wall. The evolution of domain walls from continuous undulation to a discontinuity in the columnar phase was studied in Ref. [57]. Based on numerical estimates of wall elastic energy, it was concluded that for misfit angles above 40° the density of dislocations formed at the tip of the wall becomes too large and they "melt" locally and lead to inversions of the LC director. In fact, the ±60° mosaic angle variation across the wall becomes compatible with the ±15° splay characteristic for the rest of the sample. Since director inversion requires a barrier, wall discontinuities are pinned by defects and thus rarely appear in the "normal" area of the film. The wedge is rather narrow, and bend deformation heals over a length of <0.3 μm.

Examination of the variation of the in-plane order parameter shows that the pointlike defect (b) results in the absence of dichroic signal. As it is unlikely that the strong molecular order characteristic of LCLC compounds suddenly disappears, and because we are only measuring the in-plane projection of the LC director, we conclude that the LC director rotates perpendicular to the film plane. Such an escape along the film surface normal direction seems to be essential for stabilization of wedgelike domain boundary (c), rather than the continuous melting expected in the framework of Ref. [57]. Once more, this suggests finite surface anchoring, as discussed above for the large discrepancy between the theoretical and experimental undulation period.

IV. SUMMARY

A combination of x-ray microscopy and linear dichroism NEXAFS spectroscopy was used to study texture formation in dried chromonic liquid crystal films. Through processing of different samples and analysis of fitting residuals we conclude that the procedure developed permits reconstruction of the in-plane LC director (vector along which LC molecule are aligned) with an accuracy of ~5% in the magnitude and ~5° in the orientation angle at a 100 nm scale. For both Y104 and Y105 dried films cast from concentrated solution and aligned by shear flow, it was shown there is a very high in-plane order with sinusoidal type undulations of the LC director. For the thin films studied, the period of undulation is rather large and both dyes show remarkably similar film texture. The main difference between the Y104 and Y105 species is the extent of in-plane undulation. Angular variation of the in-plane director for Y104 compound is nearly twice that for Y105. The higher spatial resolution of STXM permits detailed study of characteristic defects in LCLC films. Further development of the model of molecular packing in columnar phases needs to be developed for more quantitative data evaluation and linkage to molecular structure.

ACKNOWLEDGMENTS

This work has been supported by the Canadian Light Source through its funding partners, NSERC, CFI, and the University of Saskatchewan. This work would not have been possible without close cooperation with the Optiva, Inc. staff, in particular, M. Paukshto and N. Ovchinnikova. P.D. acknowledges CLSI financial support. Construction and operation of the STXM5.3.2 microscope is supported by NSF Grant Nos. DMR-9975694, DOE DE-FG02-98ER45737, Dow Chemical, NSERC and the Canada Foundation for Innovation. O.D.L. acknowledges partial support from NSF Grants Nos. DMR 0504516, DMR-0710544 and Samsung Electronics, Inc. We thank David Kilcoyne and Tolek Tyliszczak (both ALS) and Chithra Karunakaran and Martin Obst (CLS) for their contributions to developing and maintaining the STXM instruments and associated beamlines.

[1] J. E. Lydon, in *Handbook of Liquid Crystals*, edited by D. Demus, J. Goodby, G. W. Gray, H.-W. Speiss, and V. Vill (Wiley VCH, Weinheim, 1998), Vol. 2B p. 981–1007.
[2] J. Lydon, Curr. Opin. Colloid Interface Sci. **3**, 458 (1998).
[3] J. E. Lydon, Curr. Opin. Colloid Interface Sci. **8**, 480 (2004).
[4] T. K Attwood, J. E. Lydon, and F. Jones, Liq. Cryst. **1**, 499 (1986).
[5] V. Percec, M. Glodde, T. K. Bera, Y. Miura, I. Shiyanovskaya, K. D. Singer, V. S. K. Balagurusamy, P. A. Heiney, I. Schnell, A. Rapp, H.-W. Spiess, S. D. Hudson, and H. Duank, Nature (London) **419**, 384 (2002).
[6] F. Hoeben, P. Jonkheijm, E. W. Meijer, and A. Schenning, Chem. Rev. (Washington, D.C.) **105**, 1491 (2005).
[7] P. K. Maiti, Y. Lansac, M. A. Glaser, and N. A. Clark, Liq. Cryst. **29**, 619 (2002).
[8] A. F. Kostko, B. H. Cipriano, O. A. Pinchuk, L. Ziserman, M. A. Anisimov, D. Danino, and S. R. Raghavan, J. Phys. Chem. B **109**, 19126 (2005).
[9] J. F. Dreyer, U.S. Patent No. 2400877 (1946).
[10] L. Tortora, H.-S. Park, K. Antion, D. Finotello, and O. D. Lavrentovich, Proc. SPIE **6487**, 64801 (2007)
[11] Y. Bobrov and V. Novak, Mol. Mater. **14**, 21 (2001).
[12] M. Lavrentovich, T. Sergan, and J. Kelly, Liq. Cryst. **30**, 851 (2003).
[13] T. Sergan, T. Schneider, J. Kelly, and O. D. Lavrentovich, Liq. Cryst. **27**, 567 (2000).
[14] I. K. Iverson, S. M. Casey, W. Seo, and S-W Tam-Chang, Langmuir **18**, 3510 (2002).
[15] Yu. A. Nastishin, H. Liu, T. Schneider, V. Nazarenko, R. Vasyuta, S. V. Shiyanovskii, and O. D. Lavrentovich, Phys. Rev. E **72**, 041711 (2005).
[16] D. J. Edwards, A. P. Ormerod, G. J. T. Tiddy, A. A. Jaber, and A. Mahendrasingham, in *Physico-Chemical Principles of Color Chemistry*, edited by A. T. Peters and H. S. Freeman (Blackil Academic and Professional, Glasgow, 1996), Vol. 4, pp. 83–106.
[17] H. Ade, in *Experimental Methods in the Physical Sciences*, edited by J. A. R. Samson and D. L. Ederer (Academic Press, New York, 1998), Vol. 32, p. 225.
[18] H. Ade and S. G. Urquhart, *Chemical Applications of Synchrotron Radiation*, edited by T. K. Sham (World Scientific, Singapore, 2000).
[19] J. Stohr, *NEXAFS Spectroscopy*, Vol. 25 of Springer Series in Surface Science (Springer, Berlin, 1996).
[20] E. G. Rightor, A. P. Hitchcock, H. Ade, R. D. Leapman, S. G. Urquhart, A. P. Smith, G. Mitchell, D. Fischer, H. J. Shin, and T. Warwick, J. Phys. Chem. B **101**, 1950 (1997).
[21] I. I. Smalyukh, R. Pratibha, N. V. Madhusudana, and O. D. Lavrentovich, Eur. Phys. J. E **16**, 179 (2005).
[22] K. Severing and K. Saalwchter, Phys. Rev. Lett. **92**, 125501 (2004).
[23] K K. Kaznacheev and T. Hegmann, Phys. Chem. Chem. Phys. **9**, 1705 (2007).
[24] S. G. Urquhart, U. D. Lanke, and J. Fu, Int. J. Nanotechnol. (to be published).
[25] S. Remisov, A. Krivoshchepov, V. Nazarov, and A. Grodsky, Mol. Mater. **14**, 179 (2001).
[26] T. Schneider and O. D. Lavrentovich, Langmuir **16**, 5227 (2000).
[27] L. Ignatov, P. Lazarev, V. Nazarov, N. Ovchinnikova, and M. Paukshto, Proc. SPIE **4807**, 177 (2002).
[28] T. Schneider, K. Artyushkova, J. E. Fulghum, L. Broadwater, A. Smith, and O. D. Lavrentovich, Langmuir **21**, 2300 (2005).
[29] A. Dembo, A. Ionov, P. Lazarev, A. Manko, and V. Nazarov, Mol. Mater. **14**, 275 (2001).
[30] K. V. Kaznatcheev, Ch. Karunakaran, U. D. Lanke, S. G. Urquhart, M. Obst, and A. P. Hitchcock, Nucl. Instrum. Methods Phys. Res. A (to be published).

[31] Y. Ma, C. T. Chen, G. Meigs, K. Randall, and F. Sette, Phys. Rev. A **44**, 1848 (1991).
[32] K. C. Princea, M. Vondracek, J. Karvonen, M. Coreno, R. Camilloni, L. Avaldi, and M. de Simone, J. Electron Spectrosc. Relat. Phenom. **101-103**, 141 (1999).
[33] S. Boder and A. P. Hitchcock, Chem. Phys. **111**, 467 (1987).
[34] T. Warwick, H. Ade, A. L. D. Kilcoyne, M. Kritscher, T. Tylisczcak, S. Fakra, A. P. Hitchcock, P. Hitchcock, and H. A. Padmore, J. Synchrotron Radiat. **9**, 254 (2002).
[35] L. D. Kilcoyne, T. Tyliszczak, W. F. Steele, S. Fakra, P. Hitchcock, K. Franck, E. Anderson, B. Harteneck, E. G. Rightor, G. E. Mitchell, A. P. Hitchcock, L. Yang, T. Warwick, and H. Ade, J. Synchrotron Radiat. **102**, 125 (2003).
[36] B. Watts and H. Ade, *J. Electron Spectrosc. Relat. Phenom.* (to be published).
[37] D. Hernandez-Cruz, A. P. Hitchcock, T. Tyliszczak, Marie-Eve Rousseau, and M. Pezolet, Rev. Sci. Instrum. **78**, 033703 (2007).
[38] K. Kaznatcheev, C. Karunakuran, M. Obst, M. Sigrist, and T. Summers (unpublished).
[39] A. P. Hitchcock (unpublished).
[40] J. L. Solomon, R. J. Madix, and J. Stohr, Surf. Sci. **225**, 12 (1991).
[41] R. R. Cooney and S. G. Urquhart, J. Phys. Chem. B **108**, 18185 (2003).
[42] M. C. Gurau, D. M. Delongchamp, B. M. Vogel, E. K. Lin, D. A. Fischer, S. Sambasivan, and L. J. Richter, Langmuir **23**, 834 (2007).
[43] B. L. Henke, E. M. Gullikson, and J. C. Davis, At. Data Nucl. Data Tables **54**, 181 (1993).
[44] W. L. Jolly, K. d. Bomben, and C. J. Eyerman, At. Data Nucl. Data Tables **31**, 433 (1984).
[45] M. L. Gordon, G. Cooper, T. Araki, C. Morin, C. C. Turci, K. Kaznatcheev, and A. P. Hitchcock, J. Phys. Chem. A **107**, 6144 (2003).
[46] J. Stohr, M. G. Samant, A. Cossy-Favre, J. Diaz, Y. Momoi, S. Odahara, and T. Nagata, Macromolecules **31**, 1942 (1998).
[47] J. Stohr and M. G. Samant, J. Electron Spectrosc. Relat. Phenom. **189**, 98 (1999).
[48] L. R. Pattison, A. Hexemer, E. J. Kramer, S. Krishnan, P. M. Petroff, and D. A. Fischer, Macromolecules **39**, 2225 (2006).
[49] B. Watts, L. Thomsen, and P. C. Dastoor, J. Electron Spectrosc. Relat. Phenom. **151**, 208 (2006).
[50] P. Oswald, J. C. Geminard, L. Lejcek, and L. Sallen, J. Phys. II **6**, 281 (1996).
[51] P. G. de Gennes and J. Prost, *The Physics of Liquid Crystal* (Oxford Science, Oxford, 2006).
[52] P. Oswald and P. Pieranski, *Smectic and Columnar Liquid Crystals: Concepts and Physical Properties Illustrated by Experiments* (Taylor & Francis, New York, 2006), Chap. 9.
[53] B. I. Senyuk, I. I. Smalyukh, and O. D. Lavrentovich, Phys. Rev. E **74**, 011712 (2006).
[54] T. Schneider, A. B. Golovin, J. C. Lee, and O. D. Lavrentovich, J. Soc. Inf. Disp. **5**, 27 (2004).
[55] T. Ishikawa and O. D. Lavrentovich, Phys. Rev. E **63**, 030501(R) (2001).
[56] O. D. Lavrentovich and V. M. Pergamenshchik, Phys. Rev. Lett. **73**, 979 (1994).
[57] L. Sallen, P. Oswald, J. C. Geminard, and J. Malthete, J. Phys. II **5**, 937 (1995).